RESEARCH ARTICLE

Surface-modified Ag@Ru-P25 for photocatalytic CO$_2$ conversion with high selectivity over CH$_4$ formation at the solid–gas interface

Chaitanya B. Hiragond[1] | Sohag Biswas[2] | Niket S. Powar[1] | Junho Lee[1] |
Eunhee Gong[1] | Hwapyong Kim[1] | Hong Soo Kim[1] | Jin-Woo Jung[3] |
Chang-Hee Cho[3] | Bryan M. Wong[2] | Su-Il In[1,4]

[1]Department of Energy Science & Engineering, Daegu Gyeongbuk Institute of Science and Technology (DGIST), Daegu, Republic of Korea

[2]Department of Chemical & Environmental Engineering, Materials Science & Engineering Program, Department of Chemistry, Department of Physics & Astronomy, University of California-Riverside, Riverside, California, USA

[3]Department of Physics and Chemistry, Daegu Gyeongbuk Institute of Science and Technology (DGIST), Daegu, Republic of Korea

[4]NiceScience Corporation, Daegu, Republic of Korea

Correspondence
Bryan M. Wong, Department of Chemical & Environmental Engineering, Materials Science & Engineering Program, Department of Chemistry, Department of Physics & Astronomy, University of California-Riverside, Riverside, CA 92521, USA.
Email: bryan.wong@ucr.edu

Su-Il In, Department of Energy Science & Engineering, Daegu Gyeongbuk Institute of Science and Technology (DGIST), 333 Techno Jungang-daero, Hyeonpung-eup, Dalseong-gun, Daegu 42988, Republic of Korea.
NiceScience Corporation, 333 Techno Jungang-daero, Hyeonpung-eup, Dalseong-gun, Daegu 42988, Republic of Korea
Email: insuil@dgist.ac.kr

Funding information
Ministry of Science and ICT, South Korea, Grant/Award Number: 2021R1A2C2009459; US Department of Energy, Grant/Award Number: DE-SC0022209

Abstract
Systematic optimization of the photocatalyst and investigation of the role of each component is important to maximizing catalytic activity and comprehending the photocatalytic conversion of CO$_2$ reduction to solar fuels. A surface-modified Ag@Ru-P25 photocatalyst with H$_2$O$_2$ treatment was designed in this study to convert CO$_2$ and H$_2$O vapor into highly selective CH$_4$. Ru doping followed by Ag nanoparticles (NPs) cocatalyst deposition on P25 (TiO$_2$) enhances visible light absorption and charge separation, whereas H$_2$O$_2$ treatment modifies the surface of the photocatalyst with hydroxyl (–OH) groups and promotes CO$_2$ adsorption. High-resonance transmission electron microscopy, X-ray photoelectron spectroscopy, X-ray absorption near-edge structure, and extended X-ray absorption fine structure techniques were used to analyze the surface and chemical composition of the photocatalyst, while thermogravimetric analysis, CO$_2$ adsorption isotherm, and temperature programmed desorption study were performed to examine the significance of H$_2$O$_2$ treatment in increasing CO$_2$ reduction activity. The optimized Ag$_{1.0}$@Ru$_{1.0}$-P25 photocatalyst performed excellent CO$_2$ reduction activity into CO, CH$_4$, and C$_2$H$_6$ with a ~95% selectivity of CH$_4$, where the activity was ~135 times higher than that of pristine TiO$_2$ (P25). For the first time, this work explored the effect of H$_2$O$_2$ treatment on the photocatalyst that dramatically increases CO$_2$ reduction activity.

KEYWORDS
gas-phase CO$_2$ reduction, H$_2$O$_2$ treatment, plasmonic nanoparticles, solar fuel photocatalyst, surface modification

1 | INTRODUCTION

The increased global concentration of CO_2 in the atmosphere has sparked scientific interest in its neutralization, with a significant focus on using CO_2 as a feedstock to produce chemical fuels.[1,2] Consequently, CO_2 reduction to valuable chemical fuels (such as CO, CH_4, C_2H_6, CH_3OH, and so forth) using photocatalysts, H_2O, and solar energy has emerged as a promising technology to address the interconnected challenges of satisfying energy demand while also minimizing negative environmental repercussions.[3] In this context, the aqueous and gas phase systems have been explored for photocatalytic conversion of CO_2.[4] In an aqueous phase of CO_2 reduction, the presence of H_2O may result in a significant quantity of H_2 formation since the reduction potential for H_2O splitting requires relatively less energy than CO_2 reduction, hence hampering CO_2 reduction; however, the process that competes with H_2 formation and improves CO_2 reduction is highly demanded. Moreover, CO_2 photoreduction in the liquid phase suffers from low catalytic activity because of the limited solubility of CO_2 and difficulty in the separation of products when they could dissolve in the liquid.[5] In sharp contrast, it is anticipated that gas/vapor-phase photocatalytic CO_2 conversion with H_2O vapor utilizing a robust photocatalyst would overcome these limitations and can be an effective process in which CO_2-reduced intermediates use protons (H^+) generated by H_2O oxidation to produce hydrocarbon products.[6]

While the ability to store and transport solar energy in the form of fuel is hugely appealing, a commercially enabling photocatalyst has yet to be developed due to inherent limitations of the available photocatalyst, including limited solar light harvesting and rapid solar light harvesting charge recombination, and low stability.[7] Among numerous photocatalysts, TiO_2 has become one of the most widely studied materials for CO_2 reduction because of its cost-effectiveness and environmental benignity.[8] Its band structure provides a sufficient thermodynamic driving force that simultaneously carries CO_2 reduction and H_2O oxidation.[9] Despite these beneficial properties, it holds a large intrinsic bandgap (3.3 eV), thus showing poor light absorption in the visible region and a poor charge separation ability, resulting in poor photocatalytic activity.[10,11] As a result, several strategies such as metal/non-metal doping, vacancy formation, cocatalyst deposition, structural/facet engineering, and heterostructure formation have been devised to improve its optoelectronic (i.e., light absorption, charge separation) and surface properties (for CO_2 adsorption) to make it an efficient photocatalyst.[4] Among these, much research has focused on decorating TiO_2

with bimetal cocatalysts such as alloys, core@shell structures, and composites, for instance, Cu-Pt,[8] Au-Cu alloy,[9] Au-Pd.[10] However, synthesizing bimetal cocatalysts is challenging because their high surface energy causes metal nanoparticles (NPs) to aggregate; moreover, the role of each cocatalyst in bimetal-comprised semiconductors needs to be better understood. To alleviate such constraints, metal doping and cocatalyst deposition separately on TiO_2 would aid in systematically tuning the catalytic activity of CO_2 reduction. First, adding metal impurities into TiO_2 tunes the bandgap by creating extra defective states between valence and conduction bands, thus inducing visible light absorption. Secondly, cocatalyst deposition on such metal-doped TiO_2 acts as an electron acceptor by forming a robust Schottky junction that improves interfacial charge separation/migration for CO_2 reduction.[12] Apart from that, the adsorption of CO_2 molecules on the catalyst's surface would help to achieve improved photocatalytic activity. Surface functionalizing of TiO_2 surface by in situ grafting of basic sites to adsorb acidic CO_2 molecules is the simplest and most affordable way to increase CO_2 adsorption. For example, the surface modification of the photocatalysts with NaOH,[13] KOH,[14] halogen ions,[15] and H_2SO_4[16] has been documented in the scientific literature. To summarize, a systematic optimization of TiO_2 by metal doping, cocatalyst deposition, and surface enrichment is beneficial to increasing the efficiency of solar fuel formation.

Herein, we synthesize H_2O_2-treated Ag NPs deposited, Ru-doped P25 (TiO_2) photocatalyst (i.e., Ag@Ru-P25) and employ it for the photocatalytic reduction of CO_2 with H_2O vapors into CO, CH_4, and C_2H_6. Ru is a cost-effective dopant compared with its platinum group analogs that can extend light harvesting in the visible region by forming intermediate energy states.[17,18] Later, Ag cocatalyst deposition to Ru-P25 harvests light in the visible region by stimulating free electrons due to the plasmonic effect and improves charge separation by extracting the electrons from Ru-P25. Finally, H_2O_2 treatment on Ag@Ru-P25 enriches the surface with −OH groups that improve CO_2 adsorption. The calculated electronic structures, density function theory (DFT), and time-resolved photoluminescence (TRPL) studies demonstrate that sub-energy band levels regulate the electronic structure of the photocatalyst that facilitates increased charge separation to reduce the barrier of CO_2 reduction. In situ DRIFT analysis was used to monitor the real-time detection of the reaction intermediates to understand the reaction mechanism, and temperature programmed desorption (TPD) and other mechanistic investigations were also used to further confirm. The scientific literature has not reported a combination of photocatalysts, i.e., H_2O_2-treated

Ag-decorated Ru-doped P25 for photocatalytic CO_2 reduction. For the first time, we explored the role of surface modification of the photocatalyst with H_2O_2 treatment. This work offers the design of a simple, cost-effective, and highly efficient photocatalyst for the selective conversion of CO_2.

2 | EXPERIMENTAL

2.1 | Synthesis of Ru-doped TiO$_2$ (Ru-P25)

To synthesize Ru-P25, 10.38 mL aqueous (aq.) solution (1 mg/mL) of $RuCl_3 \cdot xH_2O$ was mixed with 500 mg P25 (TiO_2) dispersed in 30 mL deionized water. The reaction mixture was stirred for 2 h at room temperature, and the precipitate was centrifuged and copiously washed with water and ethanol three times. Then, the sample was vacuum dried in an oven for 12 h. Later, the sample was calcined in an inert atmosphere (Ar) for 5 h at 350°C using the tubular furnace. Finally, the Ru-P25 was recovered after the natural cooling of the tubular furnace. The reference samples, such as Ni, Co, and Mn-doped P25, were synthesized using a similar method by changing metal precursors.

2.2 | Synthesis of H$_2$O$_2$-treated Ag-deposited Ru-P25 (Ag@Ru-P25)

In a typical procedure, Ag deposition was carried out by an immobilization technique.[19] Here, 150 mg of as-prepared Ru-P25 was dispersed in 30 mL of deionized water and a certain amount of aq. $AgNO_3$ was introduced, and the reaction mixture was stirred for 10 min at room temperature. Then, a certain amount (i.e., wt.%) of aq. $NaBH_4$ was introduced, and the reaction mixture was stirred for 2 h at ambient conditions. The reaction mixture was centrifuged and copiously washed with deionized water three times. The as-obtained Ag@Ru-P25 sample was vacuum dried at 90°C for 12 h. Here, different weight percentages of $AgNO_3$ and $NaBH_4$ were used to obtain the deposition of Ag NPs of Ru-P25. This sample is referred to as Ag@Ru-P25$_{UT}$. To synthesize H_2O_2-modified Ag@Ru-P25, a 200 mg sample was dispersed in a 1 M solution of H_2O_2 (45 mL), and the reaction mixture was stirred for 2 h at ambient conditions. Next, the reaction mixture was washed with deionized water twice by centrifugation and vacuum dried at 80°C for 12 h.

3 | RESULTS AND DISCUSSION

3.1 | Synthesis and characterization

We have demonstrated Ag@Ru-P25 photocatalyst for the photoreduction of CO_2 into CO, CH_4, and C_2H_6 synthesized via a simple procedure. The synthesis of Ag@Ru-P25 is described in the experimental section and schematically shown in Figure S1. Field emission scanning electron microscope (FE-SEM) images of the P25, Ru-P25, and Ag$_{1.0}$@Ru-P25 samples are shown in Figure S2A–C, where no change in the morphology of the P25 was observed after Ru doping and Ag deposition. The presence of respective elements in the P25, Ru-P25, and Ag$_{1.0}$@Ru-P25 samples was confirmed by energy-dispersive X-ray spectroscopy (EDS) analysis (Figure S2D–F) and elemental mappings (Figure S2G–I). According to these results, Ru was identified in the doped sample, and Ag exhibited a good dispersion on the Ru-P25. Ultrahigh resonance transmission electron microscopy (UHR-TEM), scanning transmission electron microscopy (STEM) images, and EDS analysis were employed to confirm the formation of Ag$_{1.0}$@Ru-P25 (Figure 1). The distribution of Ag NPs on P25 can be seen in HAADF (Figure 1A) and high-resolution TEM (HR-TEM) images (Figure S3), which are confirmed by STEM images where tiny bright particles dispersed on large P25 are visible (Figure 1B). HR-TEM images have further confirmed the loading of Ag NPs on Ru-P25, as the lattice D-spacing of 0.35 and 0.23 nm correspond to anatase $TiO_2(101)$ and Ag(111) planes, respectively (Figure 1C).[20,21] Extended and inverse FFT images of Figure 1C show the lattice fringes of Ru mixing with $TiO_2(101)$ that confirm Ru doping to P25 (Figure 1D,E). Similarly, the deposition of Ag NPs on Ru-P25 can also be observed in Figure 1F,G (more information about TEM images has been provided in the Supporting Information, Figure S3). Herein, the interface between cocatalyst, that is, Ag and Ru-P25, is crucial to achieving the photo-induced charge transfer for CO_2 conversion; it can be seen that Ag NPs are closely in contact with Ru-P25, as shown in Figure S4. The elemental mapping in the Ag$_{1.0}$@Ru-P25 is shown in Figures 1H and S4D, where Ti, O, Ru, and Ag elements are present. Next, the EDS mapping of the region of interest in the Ag$_{1.0}$@Ru-P25 shows uniform distribution of Ag NPs over Ru-P25 (Figure 1I–L).

In the X-ray diffraction pattern (XRD), TiO_2 peaks corresponding to anatase and rutile are observed in all the samples; however, no peaks related to Ru or Ag were detected due to their low content (Figure S5). The peak intensity of Ru-P25 is becoming weaker than that of P25, possibly indicating decreased crystallite size of TiO_2 because of restrained crystal growth and defects formation after Ru doping.[12] Raman spectroscopy was employed to study the structural differences in P25, Ru-P25,
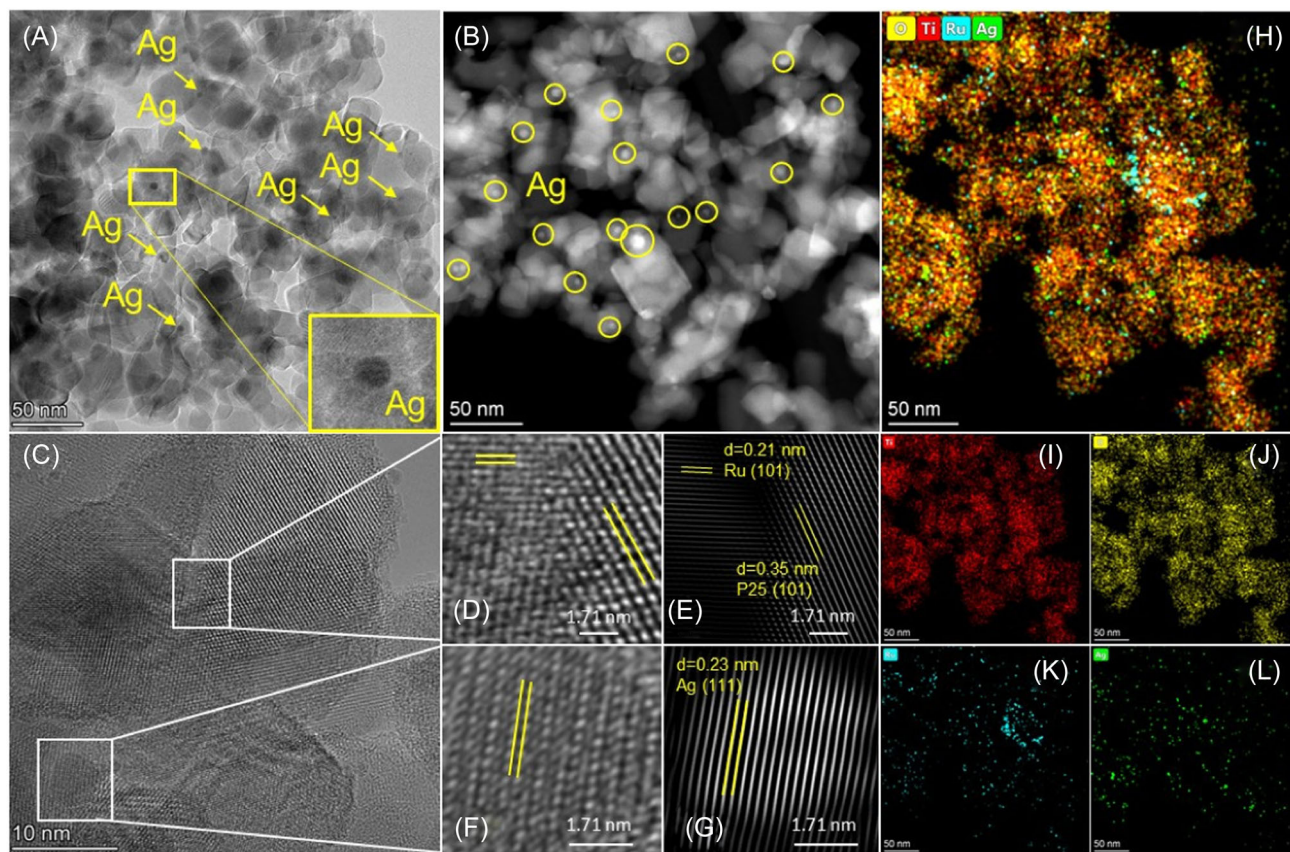
FIGURE 1 (A, B) HAADF and STEM images of $Ag_{1.0}$@Ru-P25, (C) HR-TEM image showing lattice fringes of P25 (TiO_2), Ru, and Ag in $Ag_{1.0}$@Ru-P25, (D, E) HR-TEM image of enlarged area and inverse FFT pattern of (C) showing lattice fringes of Ru and P25 (TiO_2), (F, G) HR-TEM image of enlarged area and inverse FFT pattern of (C) showing Ag NPs lattice fringes, and (H) overlap EDS mapping and (I–L) EDS mapping for Ti, O, Ru, and Ag elements, respectively, in $Ag_{1.0}$@Ru-P25.

and $Ag_{1.0}$@Ru-P25. The signals at 148.5 (E_g), 400.7 (B_{1g}), 521.5 (A_{1g}), and 634.6 (E_g) cm^{-1} correspond to Ti–O bonding in TiO_2 (Figure 2A). Ru incorporation to P25 was predicted by shifting the E_g mode from 148.5 to 157.2 cm^{-1}; peak broadening was also observed because of the inclusion of stoichiometric defects in TiO_2.[22,23] After Ag deposition, no noticeable changes were observed in the peaks of the Raman spectra. Further, the chemical states of the elements and surface compositions were analyzed by X-ray photoelectron spectroscopy (XPS) of $Ag_{1.0}$@Ru-P25 (Figures 2B–E and S6). In the high-resolution XPS spectra, Ti $2p_{3/2}$ and Ti $2p_{1/2}$ peaks belong to Ti^{4+}-O bonds of TiO_2, and the peak shift in Ru-P25 was observed after Ru incorporation (Figure S6A).[24] In the fitted Ti 2p XPS spectra of $Ag_{1.0}$@Ru-P25, the peaks at binding energies (BEs) of 457.9 and 463.80 eV correspond to Ti $2p_{3/2}$ and Ti $2p_{1/2}$ (Figure 2B). After Ru doping, Ti 2p spectra overlap with the Ru 3p,[25] and both the Ti 2p and O 1s peaks shifted toward higher BEs (Figure S6B), which can be attributed to lattice distortion in TiO_2. The electron paramagnetic resonance (EPR) measurement was performed to identify the defect states in the Ru-P25. In the

EPR spectra, the paramagnetic signals at $g = 2.05$ and 2.15 in Ru-P25 can be observed as compared with P25, which can be attributed to O vacancies and EPR active Ru^{n+} species in the sample (Figure S7).[26,27] Due to the formation of O vacancies, electron donation from O and Ti atoms occurs to maintain a charge balance at Ru-P25. In the fitted O 1s XPS spectrum of $Ag_{1.0}$@Ru-P25, the peaks related to Ti–O (TiO_2) and Ti–OH (surface hydroxyl) are present[16] (Figure 2C). Ru in $Ag_{1.0}$@Ru-P25 was confirmed by the Ru 3d core level spectrum (Figure 2D). Due to the overlapping of C 1s and Ru 3d spectra, the deconvoluted peaks at 288.1, 286.6, and 288.9 eV correspond to C 1s, while peaks at 279.6 and 285.6 eV can be designated to the Ru $3d_{5/2}$, and Ru $3d_{3/2}$ belongs to Ru^{n+} species.[12,28] After Ag NPs deposition on Ru-P25, a minor shift in the Ru 3d peaks was observed (Figure S8A). The XPS spectrum of Ag shows two peaks, $3d_{5/2}$ and $3d_{3/2}$, separated by 6.0 eV (spin energy separation) that can be attributed to Ag(0), as shown in Figure 2E.[29–32] The elemental composition of $Ag_{x\%}$@Ru-P25 is shown in Table S1, which clearly shows the Ag composition was increased according to the wt.% loading.
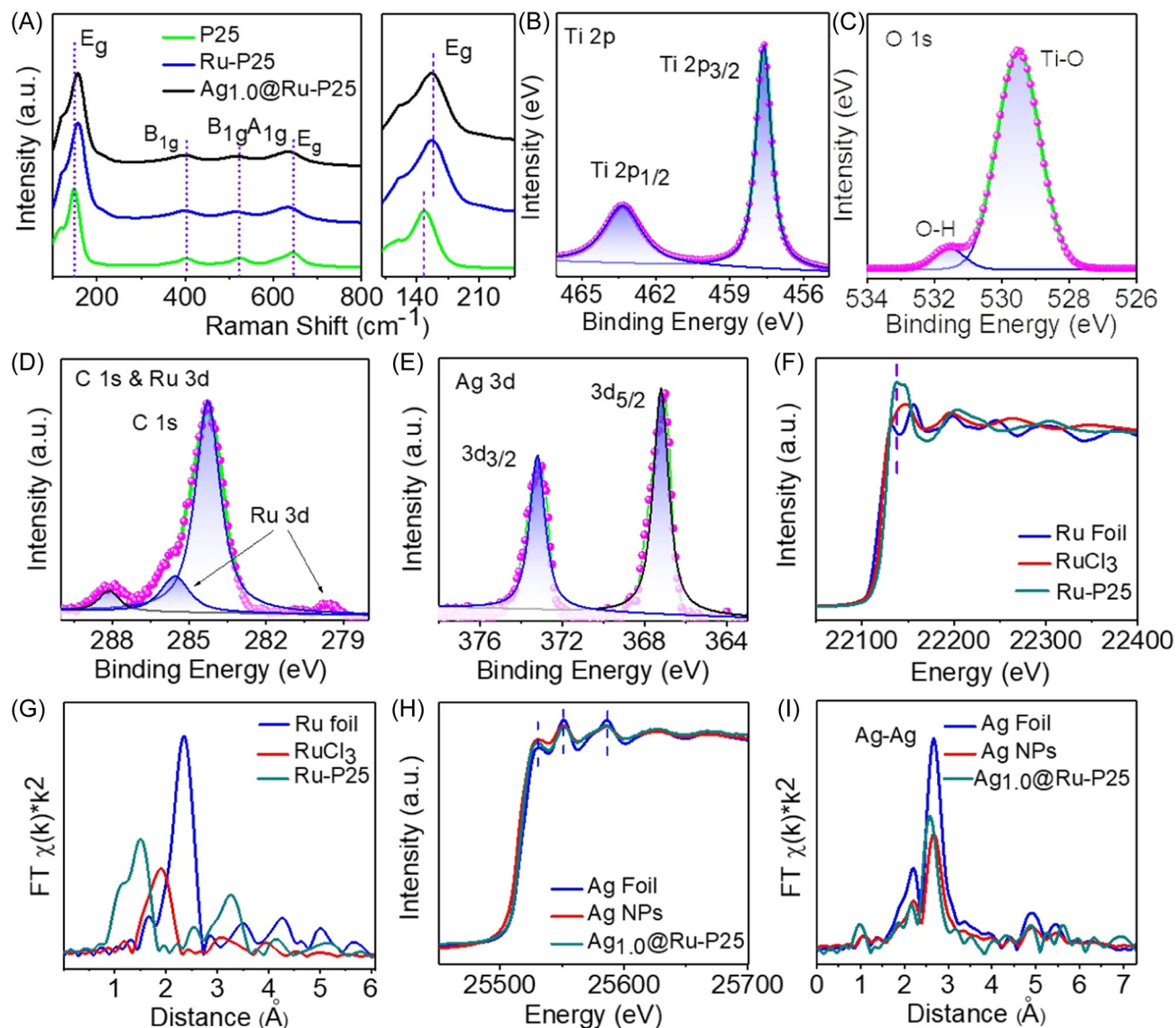
FIGURE 2 (A) Raman spectra and corresponding enlarged view of the P25, Ru-P25, and $Ag_{1.0}$@Ru-P25 samples. (B–E) High resonance XPS spectra of the $Ag_{1.0}$@Ru-P25 showing Ti 2p, O 1s, C 1s, Ru 3d, and Ag 3d, (F, G) Ru K-edge XANES and FT-EXAFS of Ru-P25 and reference samples, and (H, I) Ag K-edge XANES and FT-EXAFS of $Ag_{1.0}$@Ru-P25 and reference samples.

According to inductively coupled plasma optical emission spectroscopy (ICP-OES), the loading amount of Ag in $Ag_{x\%}$@Ru-P25 has increased from 0.5 to 2.0 wt.% (Table S2).

X-ray absorption near-edge structure (XANES) and extended X-ray absorption fine structure (EXAFS) have been conducted to explore the localized chemical environment of Ru-P25 and $Ag_{1.0}$@Ru-P25 samples. In the K-edge XANES spectra of Ru-P25, $RuCl_3$, and Ru foil, the absorption threshold of Ru in Ru-P25 approaches that of $RuCl_3$ (Figure 2F).[33] In the Fourier transformer of Ru K-edge EXAFS of the Ru-P25, the peak positions differ from the reference $RuCl_3$ and Ru foil (Figure 2G). No peak related to Ru–Ru scattering at 2.3 Å was observed in Ru-P25, ruling out metallic Ru or Ru species

aggregation. Instead, a peak at $R = 1.49$ Å corresponds to the Ru–O bond, indicating that the Ru atoms are associated with lattice neighboring O atoms.[24] The second peak at $R \sim 3.19$ Å with less intensity, corresponding to Ti-Ru, is consistent with the previous report.[28] The coordination sphere of the Ru-P25 was further quantified by EXAFS curve-fitting analyses, as shown in Figure S9A,B, where the fitted result confirmed the Ru-O bond length as 1.93 Å. The best fit of the coordination number (N) originating from the first Ru–O shell is 3.53 (Table S3). Therefore, Ru doping to TiO_2 lattice substitutes the Ti^{4+} by Ru^{n+} due to a larger ionic radius and creates oxygen vacancy (V_O), which is consistent with XPS and EPR. In the Ag K-edge XANES, scattering oscillation peaks of $Ag_{1.0}$@Ru-P25 are identical to Ag foil

and Ag NPs, confirming the presence of metallic Ag, as shown in Figure 2H. Furthermore, the Ag$_{1.0}$@Ru-P25 sample has a lower photon energy near-edge feature than Ag foil, indicating a reduced density of unoccupied Ag$_{4d/5s}$ states in the composite.[34] This result advocates an electron transfer between the Ru-P25 support and Ag NPs. In the FT-EXAFS spectra of Ag$_{1.0}$@Ru-P25, a single intense peak was obtained at $R \sim 2.7$ Å corresponding to Ag–Ag bonds, similar to the spectra of Ag NPs and foil (Figure 2I). However, the intensity of the Ag–Ag peak of Ag$_{1.0}$@Ru-P25 is weaker than that of Ag foil due to the different chemical environment of Ag with Ru-P25, and also due to the presence of Ag NPs. Such contact between two components would encourage the separation of photogenerated electron-hole pairs and promote interfacial electron transfer activities between Ru-P25 and Ag. No peaks related to Ag-O bond lengths at 1.6 Å can be observed, suggesting that the Ag NPs at the interfaces are dominantly in contact with Ti atoms and not O atoms.[34] The EXAFS data was investigated with the Ag–Ag shell fitting, as shown in Figure S9C,D. The lower k-space scattering oscillation intensity is reduced in Ag$_{1.0}$@Ru-P25 due to the nonlinear multiple scattering with heteroatoms (Figure S9D). The N$_{Ag–Ag}$ was 3.58 in Ag$_{1.0}$@Ru-P25 (Table S3), a smaller value than that in Ag foil ($N = 12$),[35] which suggests the formation of Ag NPs. Also, the R$_{Ag–Ag}$ distance in Ag$_{1.0}$@Ru-P25 (2.83 Å) is comparable to the reported value for the Ag foil (~ 2.8 Å).[35–37] The $\chi(k)$ k-weighted EXAFS of Ag$_{1.0}$@Ru-P25 showed nearly identical oscillations of Ag–Ag shell peaks to Ag foil and Ag NPs (Figure S10).[38] Additionally, the σ^2 value of Ag$_{1.0}$@Ru-P25 was higher than that of Ru-P25, indicating that disorder increases in the photocatalyst, ultimately contributing to increased photoreduction activity.

3.2 | Optical properties, electronic structure, and charge separation

UV-Vis-diffuse reflectance spectra (DRS) and valence band (VB) XPS were used to study the photocatalyst's optical properties and band alignment. In the UV-Vis-DRS, all the samples showed absorbance using <380 nm wavelength, as shown in Figure S11. Compared with P25, the Ru-P25 exhibited a significant increase in light absorption intensity ($\lambda = 400–800$ nm); Ag cocatalyst deposition onto Ru-P25 further improved the light harvesting in the visible region. As Ag concentration increased, the UV-Vis absorption further increased, meaning that Ag NPs helped to increase the light absorption in the visible region (Figure S12).[39,40] After

that, Taus's plot and VB XPS spectra were gathered to gain insight into the band structure of Ag$_{1.0}$@Ru-P25 (Figure 3A,B and Table S4). The conduction band (CB) and the VB of the P25 (-TiO$_2$) consist of Ti (3d) and O (2p) orbitals, respectively. When additional Ru ions are introduced into the lattice, the interaction between the outer shell orbitals of these ions and the energy states of the bands creates impurity levels; therefore, the Ru-P25 has decreased bandgap (3.02 eV) compared with P25 (3.28 eV) (Figure 3C).[41] Moreover, due to the charge difference between the dopant and the Ti/lattice oxygen, Ru^{n+} can compensate for the unbalanced charge by lowering charge recombination centers and generating new absorption edges, enhancing light harvesting and charge transfer. Later, Ag deposition on Ru-P25 slightly decreases the bandgap and modifies the interface band structure due to increased surface states.[40] The CB of Ag$_{1.0}$@Ru-P25 shifted slightly upward after Ag deposition due to the formation of the Schottky junction where Ag cocatalyst accepts electrons from the Ru-P25, and CO$_2$ photoreduction will occur on the metallic Ag surface due to the "surface barrier electron trapping" phenomenon. As a result, the CB and VB of Ag$_{1.0}$@Ru-P25 are defined as −1.53 and 1.40 eV, respectively, with a bandgap of 2.93 eV, which are well suitable for CO$_2$ reduction and H$_2$O oxidation simultaneously.

P25 contains both anatase and rutile TiO$_2$ structures, with anatase being more abundant. To this end, we calculated the PDOS for these TiO$_2$ structures and their composites, as shown in Figures 3D–F and S13–S18. The Fermi level of pure TiO$_2$ is 7.69 eV (Figure 3D). Introducing Ru to it creates mid-gap states, and the Fermi level shifts to 6.81 eV (Figure 3E). In particular, a new mid-gap state (Ru 4d) and O vacancies appear below the Fermi level, generating a narrow bandgap. When Ag NPs were deposited on Ru-P25, a further shift in the Fermi level to 6.52 eV was observed (Figure 3F). Specifically, O vacancies are formed, and the electron density increases on Ru-P25, which Ag NPs can extract. Therefore, the coexistence of Ru dopants, O vacancies, and Ag cocatalyst increases the charge separation in Ag@Ru-P25, which is also observed in the rutile structure (Figures S16–S18).

Photoluminescence (PL), time-resolved PL, and electrochemical analysis were conducted to investigate the interfacial charge transfer in the photocatalyst. The quenching of PL intensity in Ru-P25 than that of P25 indicates an improved photogenerated electron-hole separation in Ru-P25 (Figures 3G and S19). Ru impurities or O vacancies generated trapping states that capture the photo-excited electron and reduce the PL intensity. For Ag@Ru-P25, the PL intensity was weakest, indicating improved interfacial charge transfer and less photocarrier recombination.[40,42] In the TRPL lifetime decay, the
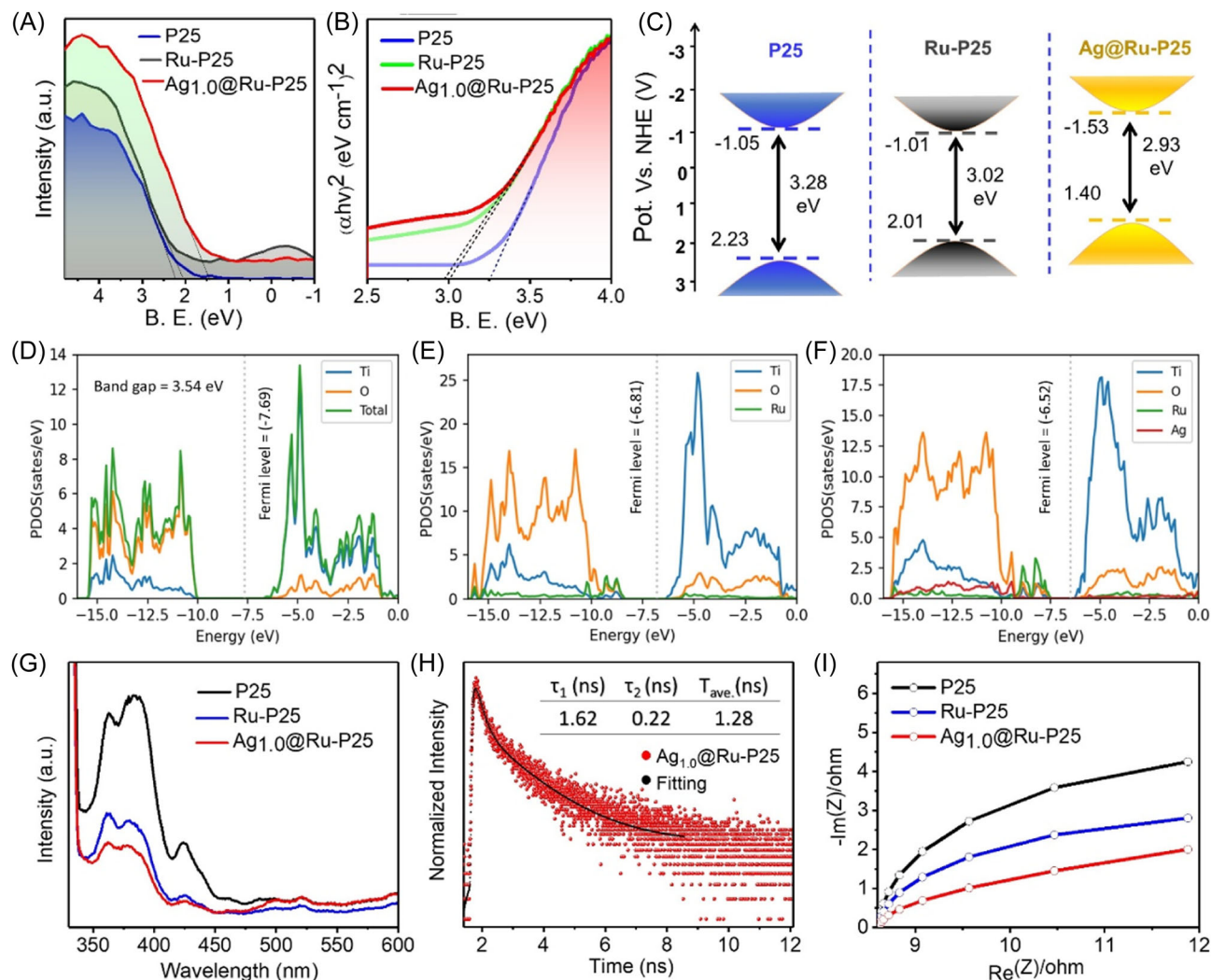
FIGURE 3 (A) Experimentally calculated bandgaps using Tauc plot, (B) VB-XPS, and (C) energy band structure for P25, Ru-P25, and $Ag_{1.0}$@Ru-P25. Partial density of states (PDOS) DFT calculations for (D) P25, (E) Ru-TiO$_2$, and (F) $Ag_{1.0}$@Ru-TiO$_2$ (Anatase TiO$_2$ [spin-up]). PDOS for rutile TiO$_2$, Ru-TiO$_2$, and Ag@Ru-TiO$_2$ are given in the Supporting Information. (G) PL spectra of P25, Ru-P25, and $Ag_{1.0}$@Ru-P25, (H) TRPL spectra of $Ag_{1.0}$@Ru-P25 (inset shows the decay lifetime), and (I) Nyquist plot for P25, Ru-P25, and $Ag_{1.0}$@Ru-P25.

charge carrier lifetimes for P25, Ru-P25, and $Ag_{1.0}$@Ru-P25 are 2.41, 2.21, and 1.28 nm, respectively (Figures S20 and 3H). The $Ag_{1.0}$@Ru-P25 has a lower lifetime of 1.28 ns compared with other samples.[43] These results confirm that the migration of photo-excited electrons is significantly faster in $Ag_{1.0}$@Ru-P25 since the trapped electrons by Ru species can be readily transferred to the Ag NPs. The electrochemical measurements further demonstrated the photocatalyst's efficient charge generation and separation (Figures S21 and 4I). The depressed semicircle of $Ag_{1.0}$@Ru-P25 compared with other samples was observed in the Nyquist plot[44,45]; the resistance of $Ag_{1.0}$@Ru-P25 is also lower than those of other samples, indicating that the charge transfer barrier is reduced at the interface of the photocatalyst and between

the electrode and electrolyte, which gradually accelerates the surface reaction.[23] These results suggest that high photocatalytic activity in $Ag_{1.0}$@Ru-P25 can be achieved due to efficient accumulation and fast transportation of electron/hole pairs via the interface.

3.3 | Photocatalytic CO$_2$ reduction

The CO$_2$ photoreduction experiments were conducted in a gas-phase setup under simulated sunlight without any photosensitizer or sacrificial agents (Figure S22 and Table S6). Here, CH$_4$ was the primary product obtained with a small amount of CO and C$_2$H$_6$ (Figure 4). Pristine P25 and Ru-P25 had significantly less CO$_2$ reduction
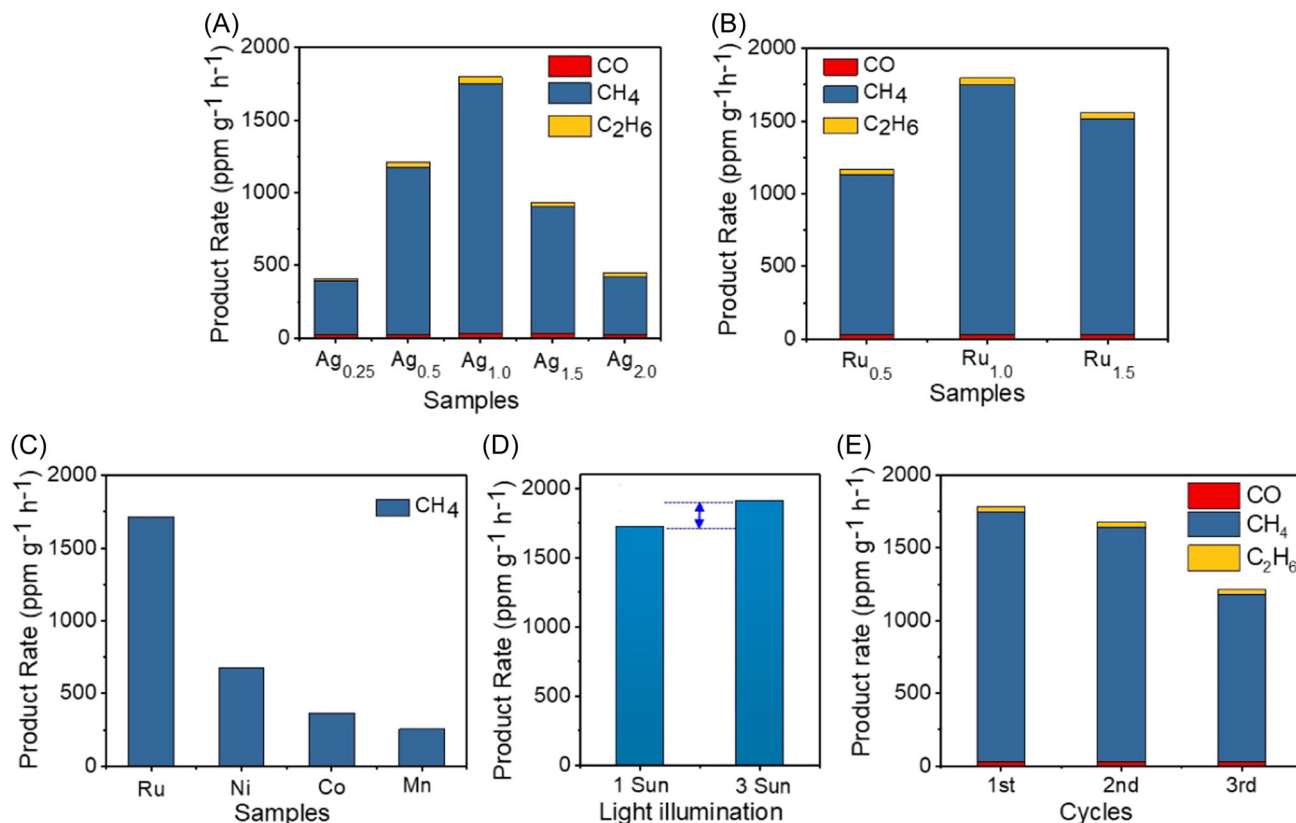
FIGURE 4 Photocatalytic CO_2 reduction of (A) $Ag_{x\%}$@Ru-P25 samples (change in Ag NPs concentration), (B) $Ag_{1.0}$@$Ru_{y\%}$-P25 (change in the Ru concentration), (C) CH_4 evolution in $Ag_{1.0}$@metal-P25 (change in metal dopant), (D) CH_4 evolution in $Ag_{1.0}$@Ru-P25 under 1- and 3-Sun illumination, and (E) stability test of $Ag_{1.0}$@Ru-P25 toward CH_4 evolution (after the first and second cycles of stability test, the sample was reactivated by simple vacuum annealing at 100°C for 2 h, which helps to retain the catalytic activity by eliminating the adsorbed intermediates occupied on active sites).

activity; therefore, the Ag cocatalyst was deposited onto Ru-P25. To get the maximum photocatalytic activity, the composition of the Ag@Ru-P25 was optimized with the different concentrations (wt.%) of Ru and Ag. The preliminary tests confirmed that an Ag@Ru-P25 with 1.0 wt.% of Ru doping and 1.0 wt.% Ag decoration promotes remarkable activity. Ag cocatalyst with different depositions on Ru-P25 showed a volcanic curve for CO_2 reduction, and improved photocatalytic activity was observed. Such improvement in the activity can be attributed to the formation of a Schottky interface, which improved charge separation in CO_2 conversion.[46] $Ag_{1.0\%}$@$Ru_{1.0}$-P25 showed CO_2 reduction into CO, CH_4, and C_2H_6 with the activity of 33.1, 1717.3, and 46.25 ppm $g^{-1} h^{-1}$ (Figure 4A), where the CH_4 selectivity was ~95% over CO and C_2H_6.

Without Ru doping, $Ag_{1.0}$@P25 produces 476.3 ppm $g^{-1} h^{-1}$ of the CH_4 (Figure S23). Therefore, the Ag cocatalyst plays a crucial role in overall photocatalytic CO_2 conversion, while Ru doping plays a minor but significant role. When Ru concentration in $Ag_{1.0}$@$Ru_{y\%}$-P25 was changed, the fluctuation in the photocatalytic

activity was observed, suggesting its relevance in photocatalysis (Figure 4B). Moreover, when Ru was replaced with other metal dopants (Figure 4C), the activity was decreased, which signifies the importance of Ru due to its n^+ oxidation state that acts as a bridge between photocatalyst and cocatalyst for efficient charge separation. Consequently, the perfect combination of catalyst and optimization of each component is responsible for getting maximum CO_2 reduction activity. The effect of multi-sun illumination was also executed, and the result suggests that the activity for CH_4 evolution increased under 3-sun illumination (Figure 4D). The increased activity could be due to (i) desorption of the product at a higher temperature (45°C recorded during the experiment) due to increased light concentration and (ii) more photons being available for the reaction to carry out. All the photocatalytic tests were performed using diluted CO_2, and the performances were relatively upright compared with several reported Ag-based catalytic systems, as shown in Table S7.

Various reference samples were also tested for CO_2 photoreduction; their activity was much less than those

of the optimal $Ag_{1.0}$@Ru-P25 (Figure S23). The $Ag_{1.0}$@Ru-P25 sample showed ~135 times higher photocatalytic activity than P25 and ~6.3, ~3.6, and ~2.4 times higher activity than various control samples for CH_4 formation, that is, $Ag_{1.0}$@P25$_{UT}$, $Ag_{1.0}$@P25, and $Ag_{1.0}$@Ru-P25$_{UT}$, respectively. Various background tests were also conducted, including (i) the absence of light illumination, (ii) dry CO_2, and (iii) replacing CO_2/H_2O with He/H_2O. No appreciable amount of these products was detected in (i) and (ii) cases, while a small amount of CH_4 was detected in the He/H_2O case (Figure S24). A $^{13}CO_2$ isotope-labeled experiment for the $Ag_{1.0}$@Ru-P25 was performed to confirm CO_2 as a carbon source. Because of its high selectivity (~95%), the CH_4 peak ($m/z = 17$) was extracted through the isotopic GCMS test (Figure S25); however, the CO and C_2H_6 peaks were not obtained, which may be referring to their lower concentrations. Thus, all these findings confirm that the product was formed by combining CO_2, H_2O, and solar light in the presence of a photocatalyst.

The stability of the $Ag_{1.0}$@Ru-P25 photocatalyst was examined for three cycles (i.e., 36 h in total), as shown in Figure 4E. After the second cycle (i.e., 24 h), the activity retained over ~96%; such stability in the gas-phase photocatalytic system is worth noting. The decreased activity in the third cycle could be attributed to (i) adsorption of intermediates on the surface of the catalyst that blocks the active sites, (iii) CO_2 chemisorption, and (iii) decrease of adsorption capacity of CO_2 and H_2O.[47–49] To further evaluate the chemical stability of the $Ag_{1.0}$@Ru-P25, the XRD and XPS analyses of the photocatalyst were collected after the reaction, as shown in Figure S26. The XRD spectrum of the tested sample (i.e., after CO_2 reduction) is identical to that of the fresh sample, demonstrating that no fresh crystals formed during the photocatalytic CO_2 reduction test (Figure S26A). In the XPS analysis, the peak positions of all the elements in the tested sample are identical to those of the fresh sample, validating the high stability of the $Ag_{1.0}$@Ru-P25 (Figure S26B–F). However, the intensity of the Ag 3d peak was decreased in the tested sample (Figure S26F) due to the adsorption of intermediates such as CO_3^{2-}, $HCOO^-$, and HCO_3^- on the surface of Ag NPs, which may block the photocatalyst's active sites. It is one of the reasons behind the decreased photocatalytic activity in the third cycle.[23]

The product selectivity of the catalytic reaction is another crucial factor in CO_2 photoreduction. The gas-phase photocatalytic reactions commonly produce H_2, CO, CH_4, and C_2H_6,[6] and the reaction carried out in the gas phase has advantages for selective reduction of CO_2 with H_2O vapor, which comparatively limits H_2 formation.[50,51] However, no H_2 was detected in the reaction, as confirmed by the gas chromatography (GC) test (Figure S29). Hence, the protons generated via H_2O oxidation during photoreaction rapidly react with intermediate carbon species from CO_2 reduction to selectively produce CH_4 that suppresses H_2 formation. The CO formation is more favorable than that of CH_4 because of the two-electron process; however, the Ag cocatalyst enriches the surface electron density, which might enhance the multielectron process to form CH_4.[52] As a result, the cocatalyst and reaction at the solid–gas interface are the components that preferentially convert CO_2 to CH_4. Therefore, the higher selectivity of CH_4 over 95% than CO and C_2H_6 on $Ag_{1.0}$@Ru-P25 was attributed to the (i) suitable band positions of the photocatalyst and (ii) the balanced CO_2 reduction and H_2O oxidation in the gas phase.

3.4 | Effect of H_2O_2 treatment on Ag@Ru-P25 toward CO_2 reduction

Another important feature of improved photocatalytic activity in $Ag_{1.0}$@Ru-P25 was the surface modification with H_2O_2. Interestingly, the photocatalytic activity of CO_2 reduction was significantly improved after H_2O_2 treatment (Figure S23), which can be attributed to two reasons: (i) it removes the carbon impurities present on the surface of the sample that activates the active surface sites, and (ii) H_2O_2 dissociates to OH^-/*OH that increases CO_2 adsorption.[14,48,53] H_2O_2 is a weak acid widely used as a cleaning agent in various applications due to its ability to remove contaminants from the surface through an oxidation process. It can significantly help to expose the active metal sites.[54] In the XPS spectra of Ag 3d, $Ag_{1.0}$@Ru-P25 has a higher peak intensity of Ag 3d than $Ag_{1.0}$@Ru-P25$_{UT}$ (Figure S8B), which can be ascribed to the exposed metallic sites after H_2O_2 treatment. A theoretical study by Lousada et al. showed such decomposition of H_2O_2 on the metal oxide surface.[55] Thetford et al. also reported H_2O_2 decomposition into 2OH forming H_2O on Au/TiO_2 surface.[56] After dissociation, the −OH group forms Ti-OOH species,[57] which is physisorbed on the catalyst's surface, resulting in surface enrichment of TiO_2. Such −OH groups can be confirmed by thermogravimetric analysis (TGA) analysis. Figure 5A shows significant weight loss in the TGA curve of Ag@Ru-P25 compared with Ag@Ru-P25$_{UT}$ (i.e., H_2O_2 untreated sample).[48] The dehydroxylation occurs at 120–500°C and corresponds to H_2O molecules from every two OH groups. Furthermore, the dissociation of H_2O_2 into OH^-/*OH modifies the photocatalyst's surface with the -OH groups,[56] which was ascribed by XPS analysis. Figure 5B,C shows the high-resolution XPS spectra of Ti $2p_{3/2}$ and O 1s peaks of $Ag_{1.0}$@Ru-P25$_{UT}$ and $Ag_{1.0}$@Ru-P25 samples, where these
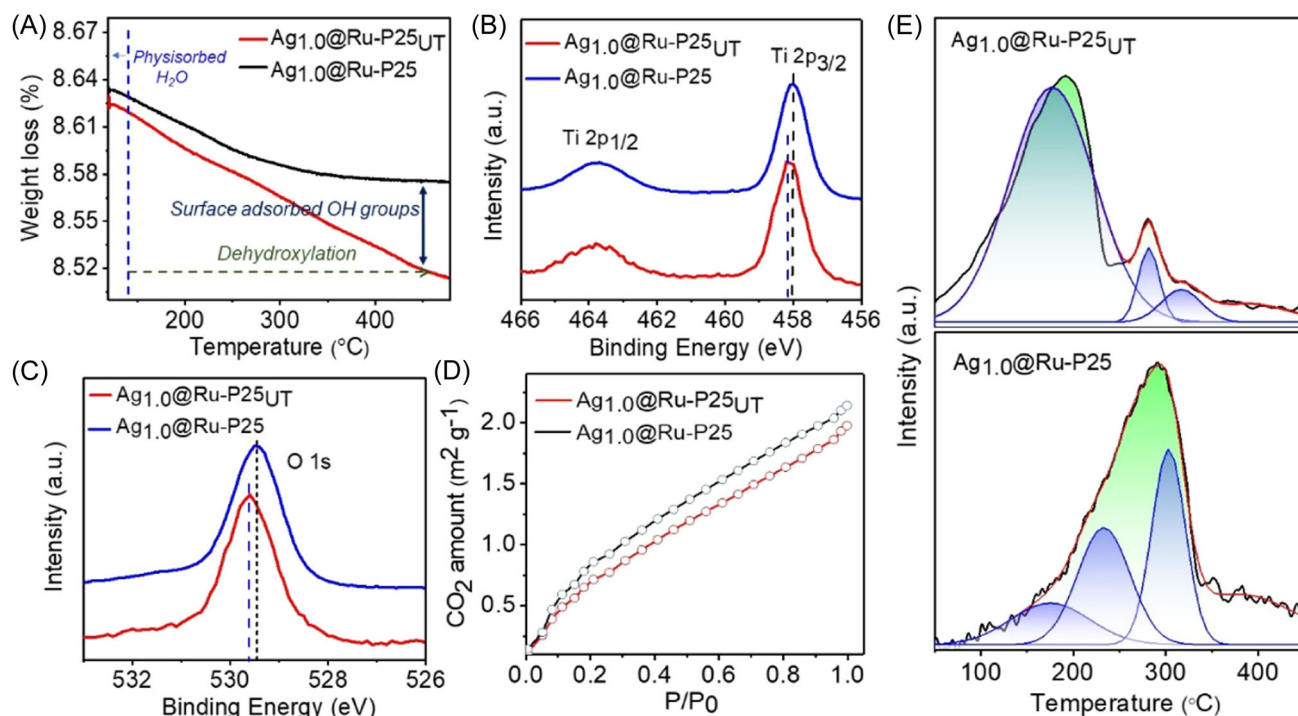
FIGURE 5 (A) TGA curves $Ag_{1.0}@Ru-P25_{UT}$ (i.e., H_2O_2 untreated) and $Ag_{1.0}@Ru-P25$, (B, C) high-resolution XPS spectra of $Ag_{1.0}@Ru-P25_{UT}$ and $Ag_{1.0}@Ru-P25$ for Ti 2p and O 1s peaks, (D) CO_2 adsorption isotherm of $Ag_{1.0}@Ru-P25_{UT}$ and $Ag_{1.0}@Ru-P25$ samples, and (E) CO_2-TPD of $Ag_{1.0}@Ru-P25_{UT}$ and $Ag_{1.0}@Ru-P25$.

peaks shifted toward lower binding energy due to surface modification. These −OH groups provide basic sites and are beneficial for the adsorption of acidic CO_2 molecules. Therefore, the CO_2 adsorption in $Ag_{1.0}@Ru-P25$ is slightly more than that in the $Ag_{1.0}@Ru-P25_{UT}$ (Figure 5D). The CO_2-TPD was analyzed to confirm the nature of the interaction of CO_2 molecules with the photocatalyst (Figure 5E). The CO_2-TPD of $Ag_{1.0}@Ru-P25_{UT}$ showed a broad peak at 50–450°C. The first dominant peak corresponds to the desorption of CO_2 from weak-strength basic sites, and such adsorption can be assigned to CO_2 adsorption with Lewis base sites.[58] The second peak was due to the interaction of CO_2 through bidentate carbonate, which was relatively weak.[59] The third desorption peak at 340°C can be assigned to CO_2 adsorption on lattice oxygen anions. However, the peaks in $Ag_{1.0}@Ru-P25$ are observed at higher desorption temperatures than those in $Ag_{1.0}@Ru-P25_{UT}$. The first peak at 50–180°C can be assigned to CO_2 species adsorption through OH groups.[60] The desorption peak at 190–250°C and 280–370°C can be assigned to CO_2 adsorption through bidentate carbonate and the presence of carboxylate or HCO_3^- intermediate species. The formation of HCO_3^- could be due to the interaction between CO_2 molecules and surface OH groups.[59] Consequently, improved and appropriate CO_2 adsorption/binding on the surface of $Ag_{1.0}@Ru-P25$ was found,

which is another important reason for enhanced photocatalytic activity.

3.5 | Mechanism of CO_2 photoreduction

For CO_2 is a highly stable linear molecule with a fully oxidized carbon atom with a high C=O bond energy of 750 kJ mol^{-1}, CO_2 photoconversion is challenging.[23,61,62] Hence, the catalyst must have the appropriate VB and CB positions to perform CO_2 photoreduction and match the reduction potential of CO_2 to CH_4.[63,64] When the $Ag_{1.0}@Ru-P25$ is irradiated under solar light, free electrons and holes can be generated. The electrons excite from the VB of P25 to the CB, leaving holes at the VB (Equation 1). The accumulated electrons from Ru-P25 transfer to deposited Ag NPs. Then accumulated electrons on the surface of the photocatalyst and "hot electrons" excited from SPR of Ag inject into CO_2, and the reduction process begins to form intermediates. At the same time, holes in the VB band of P25 carry out H_2O oxidation to produce O_2 and protons (Equation 2). The formation of O_2 was confirmed by GC with thermal conductivity detector, as shown in Figure S27. DRIFT spectroscopy was performed to identify the intermediates produced during the reaction at various time intervals on the surface of $Ag_{1.0}@Ru-P25$, as shown in Figure 6A,B.
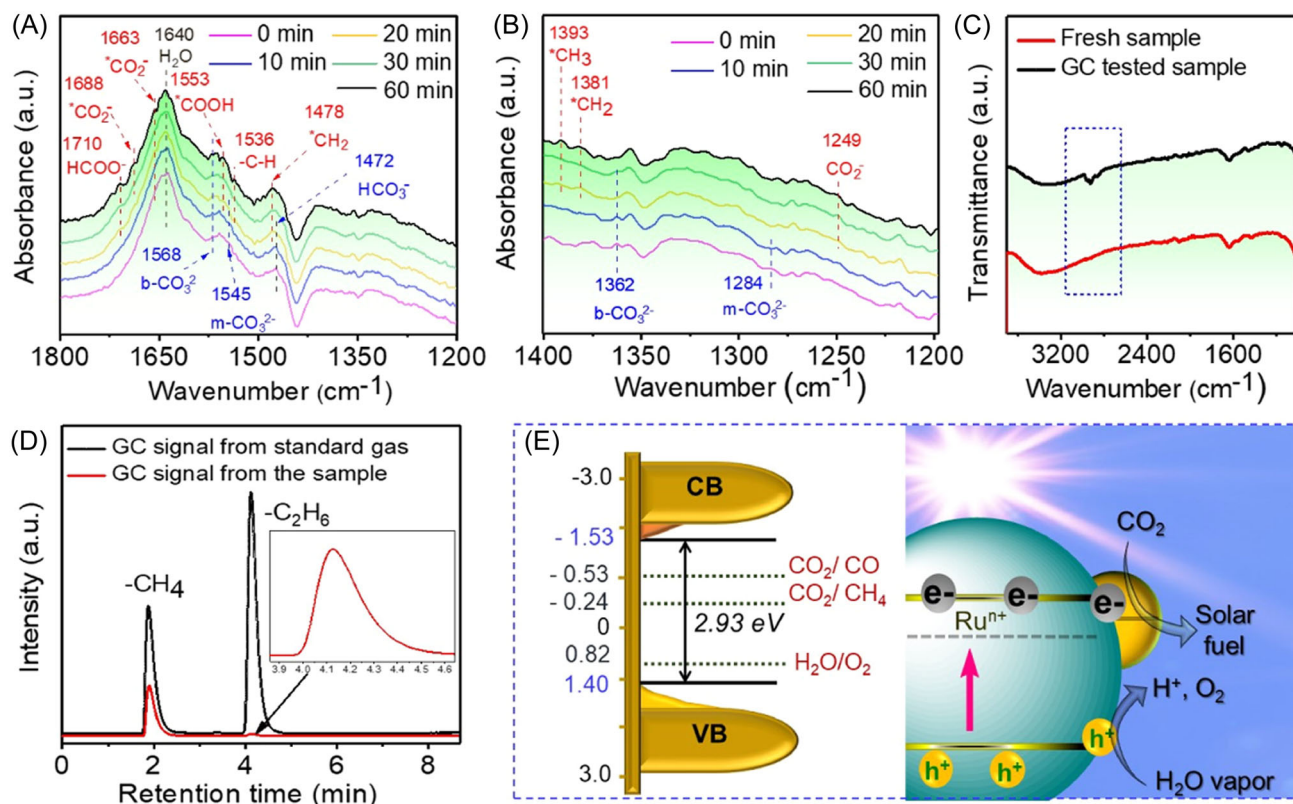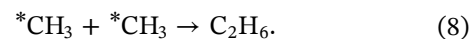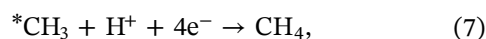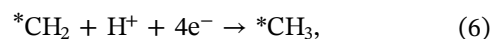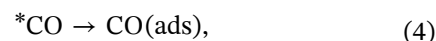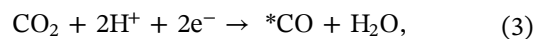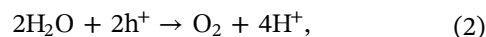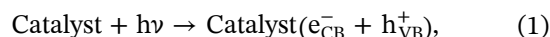
FIGURE 6 (A, B) In situ DRIFT spectra of $Ag_{1.0}$@Ru-P25 under light illumination at different time intervals and enlarged spectrum (the blue marking represents the adsorption sites and the red marking is for as-produced intermediate species), (C) FTIR spectra of $Ag_{1.0}$@Ru-P25 (fresh and tested samples CO_2 reduction), (D) GC results (obtained with flame ionization detector) of hydrocarbon evolution in $Ag_{1.0}$@Ru-P25, and (E) schematic presentation of band alignment in $Ag_{1.0}$@Ru-P25 and the proposed mechanism of CO_2 photoreduction.

The peaks related to CO_2 and H_2O adsorption through monodentate carbonate (m-CO_3^{2-} at 1284 and 1545 cm^{-1}), bidentate carbonate (b-CO_3^{2-} at 1362 and 1568 cm^{-1}), carbonate (HCO_3^- at 1472), and OH stretching (H_2O at 1640 cm^{-1}) were detected at 0 min illumination.[65,66] However, these peaks either diminish or intensities become lower after a certain time under light illumination due to conversion into various intermediate products.[67] For example, the m-CO_3^{2-} peak at 1284 cm^{-1} and HCO_3^- at 1472 cm^{-1} disappeared after 20 min illumination. On the other hand, new peaks, corresponding to CO_2^- (1249 cm^{-1}), *CO_2^- (1663 cm^{-1}), $HCOO^-$ (1710 cm^{-1}) *$COOH$ (1553 cm^{-1}), –CH stretching (1536 cm^{-1}), *CH_2 (1478 and 1375 cm^{-1}), and *CH_3 (1393 cm^{-1}), respectively, have arisen after 10–20 min illumination.[48,65,66] These peaks are the key intermediate products of the CO_2 conversion into CO, CH_4, and C_2H_6. After 60 min of light illumination, these peaks became more prominent. These findings indicate that *$COOH$ is a key intermediate to form CO, whereas *CH_3 denotes that CH_4 is formed via the proton-coupled electron transfer (PCET) process, and a few *CH_3 may react with each other to generate C_2H_6. The mechanism of the photocatalytic CO_2 reduction pathway on Ag@Ru-P25 has been predicted by the following equations:

$$Catalyst + h\nu \rightarrow Catalyst(e_{CB}^- + h_{VB}^+), \quad (1)$$

$$2H_2O + 2h^+ \rightarrow O_2 + 4H^+, \quad (2)$$

$$CO_2 + 2H^+ + 2e^- \rightarrow *CO + H_2O, \quad (3)$$

$$*CO \rightarrow CO(ads), \quad (4)$$

$$CO + 4H^+ + 4e^- \rightarrow *CH_2 + H_2O, \quad (5)$$

$$*CH_2 + H^+ + 4e^- \rightarrow *CH_3, \quad (6)$$

$$*CH_3 + H^+ + 4e^- \rightarrow CH_4, \quad (7)$$

$$*CH_3 + *CH_3 \rightarrow C_2H_6. \quad (8)$$

We have performed various mechanistic analyses to further support the in situ DRIFT results. First, the peak obtained from GC with thermal conductivity detector

validates CO formation (Figure S28); the CO is formed through $2e^- + 2H^+$ (Equations 3 and 4). Further, the accumulated electrons on the photocatalyst's surface transfer to the CO to form a *CH_3 radical with $5H^+$ and $5e^-$ through *CH_2 formation (Equations 5 and 6). The H_2 evolution by H_2O oxidation is indeed possible, but the GC tests with thermal conductivity detector excluded its formation (Figure S29); perhaps the H^+ reacts with the *CH_3 intermediates to form CH_4 (Equation 7).[67] The FTIR analysis detected *CH_3 radical by comparing the fresh and tested samples. The peaks obtained at ~2800–2960 cm^{-1} in the tested sample correspond to the C–H stretching of a *CH_3 intermediate (Figure 6C)[8,23]; such a peak is absent in the fresh sample. However, a few *CH_3 radicals may undergo dimerization to form C_2H_6 (Equation 8).[68] GC results obtained with flame ionization detector confirmed the CH_4 and C_2H_6 formations (Figure 6D). The coumarin dye test confirmed the H_2O oxidation to H^+ (Equation 2), where the as-produced *OH radicals produced during the reaction react with coumarin dye to produce highly luminescent 7-hydroxy-coumarin (Figure S30).[69] Stronger fluorescence refers to the formation/availability of more *OH radicals and perhaps more H^+ species. Based on these outcomes, a photocatalytic CO_2 reduction mechanism over band-aligned Ag@Ru-P25 has been schematically illustrated in Figure 6E.

4 | CONCLUSIONS

Ag NPs deposited Ru-P25 photocatalysts with H_2O_2 treatment exhibit the enhanced catalytic performance of CO_2 reduction toward CO, CH_4, and C_2H_6 formation. The photocatalytic activity of $Ag_{1.0}$@Ru-P25 toward CH_4 formation was ~135, ~6.3, ~3.6, and ~2.4 times higher than the P25, $Ag_{1.0}$@$P25_{UT}$, $Ag_{1.0}$@P25, and $Ag_{1.0}$@Ru-$P25_{UT}$, respectively. First, (a) Ru doping benefits the improved light absorption in visible region and charge trapping, (b) Ag cocatalyst deposited on Ru-P25 further expands light absorption and is also responsible for efficient charge separation properties due to the formation of the Schottky interface, and (c) H_2O_2 treatment was beneficial for the catalyst's surface enrichment. Secondly, the high selectivity of CH_4 over 95% was attributed to the (i) suitable band positions of the photocatalysts and (ii) the balanced CO_2 reduction and H_2O oxidation in a gas phase. The mechanism of CO_2 reduction to solar products was examined through TPD and in situ DRIFT, further strengthened by various mechanistic steps. The improved light absorption in the visible region due to bandgap narrowing, restricted electron-hole recombination by Ag cocatalyst, and surface enrichment

through H_2O_2 were responsible for the improved performance of CO_2 reduction. Our findings suggest designing simple, cost-effective, and efficient photocatalysts for solar-driven CO_2 conversion.

AUTHOR CONTRIBUTIONS

Conceptualization, guidance to prepare the manuscript and edited the manuscript: Su-Il In. Conceptualization, performed the experiments, wrote and edited the manuscript: Chaitanya B. Hiragond. Performed BET, TPD, and electrochemical analysis: Niket Powar. Performed GC-MS test: Junho Lee. Performed in-situ DRIFT analysis: Eunhee Gong. Performed H_2 evolution test: Hwapyong Kim. Performed SEM analysis; Hong Soo Kim. Performed TRPL measurements: Jin-Woo Jung and Chang-Hee Cho. Performed DFT calculations and edited the manuscript: Sohag Biswas and Bryan M. Wong.

ACKNOWLEDGMENTS

CONFLICT OF INTEREST STATEMENT

The authors declare that there are no conflicts of interests.

ORCID

Chaitanya B. Hiragond http://orcid.org/0000-0002-9408-6997
Niket S. Powar http://orcid.org/0000-0003-4024-5048
Hwapyong Kim http://orcid.org/0000-0002-9409-8218
Bryan M. Wong http://orcid.org/0000-0002-3477-8043
Su-Il In http://orcid.org/0000-0001-9063-2041

REFERENCES

1. Hiragond CB, Powar NS, Lee J, In SI. Single-atom catalysts (SACs) for photocatalytic CO_2 reduction with H_2O: activity, product selectivity, stability, and surface chemistry. *Small*. 2022;18(29):2201428.
2. Lee B-H, Gong E, Kim M, et al. Electronic interaction between transition metal single-atoms and anatase TiO_2 boosts CO_2 photoreduction with H_2O. *Energy Environ Sci*. 2022;15(2):601-609.
3. Ma Y, Wang X, Jia Y, Chen X, Han H, Li C. Titanium dioxide-based nanomaterials for photocatalytic fuel generations. *Chem Rev*. 2014;114(19):9987-10043.

4. Gong E, Ali S, Hiragond CB, et al. Solar fuels: research and development strategies to accelerate photocatalytic CO_2 conversion into hydrocarbon fuels. *Energy Environ Sci.* 2022;15(3):880-937.

5. Li H, Cheng C, Yang Z, Wei J. Encapsulated CdSe/CdS nanorods in double-shelled porous nanocomposites for efficient photocatalytic CO_2 reduction. *Nat Commun.* 2022; 13:6466.

6. Hiragond CB, Lee J, Kim H, Jung J-W, Cho C-H, In S-I. A novel n-doped graphene oxide enfolded reduced titania for highly stable and selective gas-phase photocatalytic CO_2 reduction into CH_4: an in-depth study on the interfacial charge transfer mechanism. *Chem Eng J.* 2021;416:127978.

7. Asahi R, Morikawa T, Irie H, Ohwaki T. Nitrogen-doped titanium dioxide as visible-light-sensitive photocatalyst: designs, developments, and prospects. *Chem Rev.* 2014;114(19):9824-9852.

8. Sorcar S, Hwang Y, Lee J, et al. CO_2, water, and sunlight to hydrocarbon fuels: a sustained sunlight to fuel (joule-to-joule) photoconversion efficiency of 1%. *Energy Environ Sci.* 2019;12(9):2685-2696.

9. Liu Q, Chen Q, Li T, et al. Vacancy engineering of AuCu cocatalysts for improving the photocatalytic conversion of CO_2 to CH_4. *J Mater Chem A.* 2019;7(47):27007-27015.

10. Ziarati A, Badiei A, Luque R, Dadras M, Burgi T. Visible light CO_2 reduction to CH_4 using hierarchical yolk@shell $TiO_{2-x}H_x$ modified with plasmonic Au–Pd nanoparticles. *ACS Sustainable Chem Eng.* 2020;8(9):3689-3696.

11. Das S, Pérez-Ramírez J, Gong J, et al. Core–shell structured catalysts for thermocatalytic, photocatalytic, and electrocatalytic conversion of CO_2. *Chem Soc Rev.* 2020;49(10):2937-3004.

12. Ismael M. Highly effective ruthenium-doped TiO_2 nanoparticles photocatalyst for visible-light-driven photocatalytic hydrogen production. *New J Chem.* 2019;43(24):9596-9605.

13. Meng X, Ouyang S, Kako T, et al. Photocatalytic CO_2 conversion over alkali modified TiO_2 without loading noble metal cocatalyst. *Chem Commun.* 2014;50(78):11517-11519.

14. Ye M, Wang X, Liu E, Ye J, Wang D. Boosting the photocatalytic activity of P25 for carbon dioxide reduction by using a surface-alkalinized titanium carbide MXene as cocatalyst. *ChemSusChem.* 2018;11(10):1606-1611.

15. Hao L, Kang L, Huang H, et al. Surface-halogenation-induced atomic-site activation and local charge separation for superb CO_2 photoreduction. *Adv Mater.* 2019;31(25):1900546.

16. He Z, Tang J, Shen J, Chen J, Song S. Enhancement of photocatalytic reduction of CO_2 to CH_4 over TiO_2 nanosheets by modifying with sulfuric acid. *Appl Surf Sci.* 2016;364: 416-427.

17. Zhang H, Wu X, Chen C, et al. Spontaneous ruthenium doping in hierarchical flower-like Ni_2P/NiO heterostructure nanosheets for superb alkaline hydrogen evolution. *Chem Eng J.* 2021;417:128069.

18. Nguyen-Phan T-D, Luo S, Vovchok D, et al. Three-dimensional ruthenium-doped TiO_2 sea urchins for enhanced visible-light-responsive H_2 production. *Phys Chem Chem Phys.* 2016;18(23):15972-15979.

19. Jiang Z, Ouyang Q, Peng B, Zhang Y, Zan L. Ag size-dependent visible-light-responsive photoactivity of Ag–TiO_2 nanostructure based on surface plasmon resonance. *J Mater Chem A.* 2014;2(46):19861-19866.

20. Li N, Cai Y, Shen Q, Zhou J. Metal–organic framework-templated synthesis of Ag/Ni-TiO_2 for enhanced photocatalytic CO_2 reduction. *J Photonics Energy.* 2019;10(2):23502.

21. Sorcar S, Thompson J, Hwang Y, et al. High-rate solar-light photoconversion of CO_2 to fuel: controllable transformation from C_1 to C_2 products. *Energy Environ Sci.* 2018;11(11): 3183-3193.

22. Martínez Tejada LM, Muñoz A, Centeno MA, Odriozola JA. In-situ Raman spectroscopy study of Ru/TiO_2 catalyst in the selective methanation of CO. *J Raman Spectrosc.* 2016;47(2): 189-197.

23. Pan H, Wang X, Xiong Z, Sun M, Murugananthan M, Zhang Y. Enhanced photocatalytic CO_2 reduction with defective TiO_2 nanotubes modified by single-atom binary metal components. *Environ Res.* 2021;198:111176.

24. Zhang H, Zuo S, Qiu M, et al. Direct probing of atomically dispersed ru species over multi-edged TiO_2 for highly efficient photocatalytic hydrogen evolution. *Sci Adv.* 2020;6(39):eabb9823.

25. Ouyang W, Muñoz-Batista MJ, Kubacka A, Luque R, Fernández-García M. Enhancing photocatalytic performance of TiO_2 in H_2 evolution via ru co-catalyst deposition. *Appl Catal B.* 2018;238:434-443.

26. Nong S, Dong W, Yin J, et al. Well-dispersed ruthenium in mesoporous crystal TiO_2 as an advanced electrocatalyst for hydrogen evolution reaction. *J Am Chem Soc.* 2018;140(17): 5719-5727.

27. Zhang D, Sun Y, Tian X, et al. Promoting photocatalytic CO_2 reduction to CH_4 via a combined strategy of defects and tunable hydroxyl radicals. *J Colloid Interface Sci.* 2022;606: 1477-1487.

28. Li J, Yi D, Zhan F, et al. Monolayered Ru_1/TiO_2 nanosheet enables efficient visible-light-driven hydrogen evolution. *Appl Catal B.* 2020;271:118925.

29. Zhao S, Chen J, Liu Y, et al. Silver nanoparticles confined in shell-in-shell hollow TiO_2 manifesting efficiently photocatalytic activity and stability. *Chem Eng J.* 2019;367:249-259.

30. Tan D, Zhang J, Shi J, et al. Photocatalytic CO_2 transformation to CH_4 by Ag/Pd bimetals supported on n-doped TiO_2 nanosheet. *ACS Appl Mater Interfaces.* 2018;10(29): 24516-24522.

31. Wang J, Wang J, Li N, et al. Direct z-scheme 0D/2D heterojunction of $CsPbBr_3$ quantum dots/Bi_2WO_6 nanosheets for efficient photocatalytic CO_2 reduction. *ACS Appl Mater Interfaces.* 2020;12(28):31477-31485.

32. Yang D, Sun Y, Tong Z, Tian Y, Li Y, Jiang Z. Synthesis of Ag/TiO_2 nanotube heterojunction with improved visible-light photocatalytic performance inspired by bioadhesion. *J Phys Chem C.* 2015;119(11):5827-5835.

33. Liu Z, Zhang F, Rui N, et al. Highly active ceria-supported ru catalyst for the dry reforming of methane: in situ identification of $Ru^{\delta+}$–Ce^{3+} interactions for enhanced conversion. *ACS Catal.* 2019;9(4):3349-3359.

34. Zhou J, Tian G, Chen Y, et al. Synthesis of hierarchical TiO_2 nanoflower with anatase–rutile heterojunction as ag support for efficient visible-light photocatalytic activity. *Dalton Trans.* 2013;42(31):11242-11251.

35. Ruan H, Nishibori M, Uchiyama T, et al. Soot oxidation performance with a HZSM-5 supported ag nanoparticles catalyst and the characterization of ag species. *RSC Adv.* 2017;7(69):43789-43797.

36. Herzog A, Bergmann A, Jeon HS, et al. Operando investigation of ag-decorated Cu_2O nanocube catalysts with enhanced CO_2 electroreduction toward liquid products. *Angew Chem Int Ed.* 2021;60(13):7426-7435.

37. López-Hernández I, Truttmann V, Garcia C, et al. AgAu nanoclusters supported on zeolites: structural dynamics during CO oxidation. *Catal Today.* 2022;384-386: 166-176.

38. Wang Z, Teramura K, Hosokawa S, Tanaka T. Highly efficient photocatalytic conversion of CO_2 into solid CO using H_2O as a reductant over ag-modified $ZnGa_2O$ 4. *J Mater Chem A.* 2015;3(21):11313-11319.

39. Ratchford DC. Plasmon-induced charge transfer: challenges and outlook. *ACS Nano.* 2019;13(12):13610-13614.

40. Collado L, Reynal A, Fresno F, et al. Unravelling the effect of charge dynamics at the plasmonic metal/semiconductor interface for CO_2 photoreduction. *Nat Commun.* 2018;9: 4986.

41. Xie W, Li R, Xu Q. Enhanced photocatalytic activity of se-doped TiO_2 under visible light irradiation. *Sci Rep.* 2018; 8(1):8752.

42. Li B, Wei F, Su B, et al. Mesoporous cobalt tungstate nanoparticles for efficient and stable visible-light-driven photocatalytic CO_2 reduction. *Mater Today Energy.* 2022;24:100943.

43. Su B, Huang H, Ding Z, Roeffaers MBJ, Wang S, Long J. S-scheme $CoTiO_3/Cd_{9.51}Zn_{0.49}S_{10}$ heterostructures for visible-light driven photocatalytic CO_2 reduction. *J Mater Sci Technol.* 2022;124:164-170.

44. Wang Y, Liu XH, Wang Q, et al. Insights into charge transfer at an atomically precise nanocluster/semiconductor interface. *Angew Chem.* 2020;132(20):7822-7828.

45. Wang R, Yang P, Wang S, Wang X. Distorted carbon nitride nanosheets with activated n→ π* transition and preferred textural properties for photocatalytic CO_2 reduction. *J Catal.* 2021;402:166-176.

46. Zhang Y, Zhou S, Su X, et al. Synthesis and characterization of ag-loaded p-type TiO_2 for adsorption and photocatalytic degradation of tetrabromobisphenol A. *Water Environ Res.* 2020;92(5):713-721.

47. Sorcar S, Hwang Y, Grimes CA, In S-I. Highly enhanced and stable activity of defect-induced titania nanoparticles for solar light-driven CO_2 reduction into CH_4. *Mater Today.* 2017;20(9):507-515.

48. Kharade AK, Chang S. Contributions of abundant hydroxyl groups to extraordinarily high photocatalytic activity of amorphous titania for CO_2 reduction. *J Phys Chem C.* 2020;124(20):10981-10992.

49. Tang Q, Xiong P, Wang H, Wu Z. Boosted CO_2 photoreduction performance on $Ru-Ti_3CN$ MXene-TiO_2 photocatalyst synthesized by non-HF lewis acidic etching method. *J Colloid Interface Sci.* 2022;619:179-187.

50. Kong Z-C, Liao J-F, Dong Y-J, et al. Core@shell $CsPbBr_3$@zeolitic imidazolate framework nanocomposite for efficient

51. photocatalytic CO_2 reduction. *ACS Energy Lett.* 2018;3(11): 2656-2662.

51. Xie S, Wang Y, Zhang Q, Deng W, Wang Y. MgO-and pt-promoted TiO_2 as an efficient photocatalyst for the preferential reduction of carbon dioxide in the presence of water. *ACS Catal.* 2014;4(10):3644-3653.

52. Feng X, Pan F, Tran BZ, Li Y. Photocatalytic CO_2 reduction on porous TiO_2 synergistically promoted by atomic layer deposited MgO overcoating and photodeposited silver nanoparticles. *Catal Today.* 2020;339:328-336.

53. Liu L, Zhao C, Miller JT, Li Y. Mechanistic study of CO_2 photoreduction with H_2O on Cu/TiO_2 nanocomposites by in situ X-ray absorption and infrared spectroscopies. *J Phys Chem C.* 2017;121(1):490-499.

54. Aguinaco A, Pocostales JP, García-Araya JF, Beltrán FJ. Decomposition of hydrogen peroxide in the presence of activated carbons with different characteristics. *J Chem Technol Biotechnol.* 2011;86(4):595-600.

55. Lousada CM, Johansson AJ, Brinck T, Jonsson M. Mechanism of H_2O_2 decomposition on transition metal oxide surfaces. *J Phys Chem C.* 2012;116(17):9533-9543.

56. Thetford A, Hutchings GJ, Taylor SH, Willock DJ. The decomposition of H_2O_2 over the components of Au/TiO_2 catalysts. *Proc R Soc A Math Phys Eng Sci.* 2011;467(2131): 1885-1899.

57. Meng F, Zhang S, Zeng Y, et al. Promotional effect of surface fluorine on TiO_2: catalytic conversion of O_3 and H_2O_2 into OH and O_2^- radicals for high-efficiency NO oxidation. *Chem Eng J.* 2021;424:130358.

58. Wang Z-W, Wan Q, Shi Y-Z, et al. Selective photocatalytic reduction CO_2 to CH_4 on ultrathin TiO_2 nanosheet via coordination activation. *Appl Catal B.* 2021;288:120000.

59. Li W, Jin L, Gao F, et al. Advantageous roles of phosphate decorated octahedral CeO_2 {111}/g-C_3N_4 in boosting photocatalytic CO_2 reduction: charge transfer bridge and lewis basic site. *Appl Catal B.* 2021;294:120257.

60. Wang H, Zhang L, Wang K, Sun X, Wang W. Enhanced photocatalytic CO_2 reduction to methane over $WO_{3-0.33}H_2O$ via mo doping. *Appl Catal B.* 2019;243:771-779.

61. Park YH, Kim D, Hiragond CB, et al. Phase-controlled 1T/2H-MoS_2 interaction with reduced TiO_2 for highly stable photocatalytic CO_2 reduction into CO. *J CO2 Util.* 2023;67:102324.

62. Hiragond C, Kim H, Lee J, Sorcar S, Erkey C, In S-I. Electrochemical CO_2 reduction to CO catalyzed by 2D nanostructures. *Catalysts.* 2020;10(1):98.

63. Hiragond C, Ali S, Sorcar S, In S-I. Hierarchical nanostructured photocatalysts for CO_2 photoreduction. *Catalysts.* 2019;9(4):370.

64. Hiragond CB, Powar NS, In S-I. Recent developments in lead and lead-free halide perovskite nanostructures towards photocatalytic CO_2 reduction. *Nanomaterials.* 2020;10(12):2569.

65. Yu Y, Dong X, Chen P, et al. Synergistic effect of Cu single atoms and Au–Cu alloy nanoparticles on TiO_2 for efficient CO_2 photoreduction. *ACS Nano.* 2021;15(9): 14453-14464.

66. Cai S, Zhang M, Li J, Chen J, Jia H. Anchoring single-atom Ru on CdS with enhanced CO_2 capture and charge accumulation

for high selectivity of photothermocatalytic CO_2 reduction to solar fuels. *Solar RRL*. 2020;5(2):2000313.

67. Chen G, Wei F, Zhou Z, et al. Phase junction crystalline carbon nitride nanosheets modified with CdS nanoparticles for photocatalytic CO_2 reduction. *Sustainable Energy Fuels*. 2023;7(2):381-388.

68. Vahidzadeh E, Zeng S, Manuel AP, et al. Asymmetric multipole plasmon-mediated catalysis shifts the product selectivity of CO_2 photoreduction toward C_{2+} products. *ACS Appl Mater Interfaces*. 2021;13(6):7248-7258.

69. Ali S, Lee J, Kim H, et al. Sustained, photocatalytic CO_2 reduction to CH_4 in a continuous flow reactor by earth-abundant materials: reduced titania-Cu_2O z-scheme hetero-structures. *Appl Catal B*. 2020;279:119344.

SUPPORTING INFORMATION

Additional supporting information can be found online in the Supporting Information section at the end of this article.